

The DECam Minute Cadence Survey I.

Claudia Belardi^{1,2}, Mukremin Kilic¹, Jeffrey A. Munn³, A. Gianninas¹,
Sara D. Barber^{1,6}, Arjun Dey⁴, Peter B. Stetson⁵

¹*Homer L. Dodge Department of Physics and Astronomy, University of Oklahoma, 440 W. Brooks St., Norman, OK 73019, USA*

²*Department of Physics and Astronomy, University of Leicester, University Road, Leicester LE1 7RH, UK*

³*US Naval Observatory, Flagstaff Station, 10391 W. Naval Observatory Road, Flagstaff, AZ 86005, USA*

⁴*National Optical Astronomy Observatory, 950 N. Cherry Ave., Tucson, AZ 85719, USA*

⁵*Dominion Astrophysical Observatory, NRC-Herzberg, 5071 West Saanich Road, Victoria, BC V9E 2E7, Canada*

⁶*American Institute of Physics Congressional Fellow*

4 October 2018

ABSTRACT

We present the first results from a minute cadence survey of a three square degree field obtained with the Dark Energy Camera. We imaged part of the Canada–France–Hawaii Telescope Legacy Survey area over eight half-nights. We use the stacked images to identify 111 high proper motion white dwarf candidates with $g \leq 24.5$ mag and search for eclipse-like events and other sources of variability. We find a new $g = 20.64$ mag pulsating ZZ Ceti star with pulsation periods of 11–13 min. However, we do not find any transiting planetary companions in the habitable zone of our target white dwarfs. Given the probability of eclipses of 1% and our observing window from the ground, the non-detection of such companions in this first field is not surprising. Minute cadence DECam observations of additional fields will provide stringent constraints on the frequency of planets in the white dwarf habitable zone.

Key words: techniques: photometric – eclipses – white dwarfs.

1 INTRODUCTION

Transient surveys like the Palomar Transient Factory (Rau et al. 2009), Panoramic Survey Telescope & Rapid Response System Medium Deep Fields (Kaiser et al. 2010; Tonry et al. 2012), Dark Energy Survey Supernova Fields (Flaugher 2005; Bernstein et al. 2012), Sloan Digital Sky Survey Stripe 82 (Ivezić et al. 2007), Catalina surveys (Drake et al. 2009), as well as microlensing surveys like the Massive Compact Halo Objects project (Alcock et al. 2000) and the Optical Gravitational Lensing Experiment (Udalski 2003) have targeted large areas of the sky with hour to day cadences to identify variable objects like supernovae, novae, Active Galactic Nuclei, cataclysmic variables, eclipsing and contact binaries, and microlensing events.

Several exoplanet surveys, e.g., the Wide Angle Search for Planets (WASP) and Hungarian-made Automated Telescope Network (HATNet), have used a number of small cameras or telescopes to obtain \sim few min cadence photometry on a large number of stars, providing 1% photometry for stars brighter than 12 mag. Yet other transient surveys targeted specific types of stars, like M dwarfs for the MEarth project, to look for exoplanets around them. The largest exoplanet survey so far, the Kepler mission, pro-

vided short cadence (≈ 1 min) data for 512 targets in the original mission, and the ongoing K2 mission is adding several dozen more short cadence targets for each new field observed. One of the unusual findings from the Kepler/K2 mission includes an exciting discovery of a disintegrating planetesimal around the dusty white dwarf WD 1145+017 in a 4.5 h orbit (Vanderburg et al. 2015; Gänsicke et al. 2016; Rappaport et al. 2016). Such planetesimals around white dwarfs have not been found before because none of the previous surveys were able to observe a large number of white dwarfs for an extended period of time. These planetesimals are likely sent closer to the central star through planet-planet interactions (Jura 2003; Debes, Walsh & Stark 2012; Veras et al. 2013). Hence, at least some planets must survive the late stages of stellar evolution.

The Large Synoptic Survey Telescope (LSST) will identify about 13 million white dwarfs and it will provide repeated observations of the southern sky every 3 days over a period of 10 years. Each LSST visit consists of two 15 s exposures, reaching a magnitude limit of $g = 24.5$ mag. However, this cadence is not optimum for identifying sources that vary on minute timescales. Here we present the first results from a new minute-cadence survey on the Cerro Tololo 4m Blanco Telescope that reaches the same magnitude limit as each of

the LSST visits. We take advantage of the relatively large field of view of the Dark Energy Camera (DECam, Flaugher 2005) to perform eight half-night long observations of individual fields to explore the variability of the sky in minute timescales.

For this paper, we focus on the 111 high proper motion white dwarf candidates in our first survey field. We describe the details of our observations and reductions in Section 2. Sections 3 and 4 provide proper motion measurements and the sample properties. We present the light curves for the variable white dwarfs in Section 5, and conclude in Section 6.

2 DECAM DATA

2.1 Observations

We used DECam mounted on the Blanco 4m Telescope on UT 2014 Feb 2-9 to obtain g -band exposures of a three square degree field (corresponding to a single DECam pointing) centred at Right Ascension $\alpha = 9\text{h } 3\text{m } 2\text{s}$ and Declination $\delta = -4\text{d } 35\text{m } 0\text{s}$. Our observations were performed under the NOAO program 2014A-0073. This field was previously observed by the Canada-France-Hawaii Telescope Legacy Survey (CFHTLS¹) between 2003 and 2008, and is part of the CFHTLS Wide 2 field, which is a 25 square degree field with MegaCam $ugriz$ photometry available. The earlier MegaCam data provide the first epoch for our proper motion measurements.

DECam consists of a grid of 62 CCDs, each with size 2048×4096 pixels and platescale $0.263''$ per pixel. However, two of the CCDs were not functioning during our observing run, reducing the number of usable CCDs to 60.

All of our observations were obtained during the second half-of-the night, resulting in 4 hour long observing windows each night. The airmass of the target field ranged from 1.1 to 2.5 with a median airmass of 1.3 for the entire run. The g -band seeing ranged from 0.97 to $2.08''$, with a median seeing of $1.23''$. Given the change in seeing, the individual exposure times ranged from 70 to 90 s, leading to an overall cadence of ≈ 90 to 110 s due to the ≈ 20 s read-out time of the camera. These exposure times were chosen to obtain $S/N \geq 5$ photometry of targets brighter than $g = 24.5$ AB mag under the different seeing conditions. We obtained a total of 1041 DECam images of this field.

2.2 Data Reduction

We downloaded the reduced and calibrated DECam images from the NOAO Science Archive. Our images were processed through the NOAO ‘‘Community Pipeline’’ (version 3.0.2), as described in the NOAO Data Handbook² (2015). The pipeline uses calibration exposures taken during the observing run, such as biases and dome-flats, to remove the instrumental signature, and applies astrometric and photometric calibrations. The dark current in DECam is extremely low, and no dark correction is applied in the pipeline.

The 2MASS³ source positions are used as a reference to perform the initial astrometric correction. Initial photometric calibration and estimates of the zero-point magnitudes for the science images were obtained by comparing the DECam instrumental brightnesses of field stars to their published magnitudes in the USNO-B1 catalog (Monet et al. 2003).

3 HIGH PROPER MOTION WHITE DWARFS

3.1 Proper Motions

The CFHT Legacy Survey Wide 2 field is a low-extinction, $E(B - V) = 0.02$ mag, $4.8^\circ \times 4.7^\circ$ field located at a Galactic latitude of $l = +26.6^\circ$. The MegaCam data on this field reach a completeness limit of $g = 25.5$ mag. In order to reach a comparable or better limiting magnitude, we stack 706 of our DECam images with airmass < 1.5 and a median seeing of $1.16''$. We stack the images on a chip by chip basis using the IRAF *imcombine* package, and trim off the bad portions of each image, especially near the chip edges.

We used SExtractor (Bertin & Arnouts 1996) to detect objects in the stacked image, and measured their positions (based on the windowed first order moments of the image profile, XWIN_IMAGE and YWIN_IMAGE) and instrumental magnitudes. These were matched to the CFHT Legacy Survey (CFHTLS) Wide 2 Field from the Terapix T0007 data release. In order to derive absolute proper motions, we calibrated the DECam astrometry against the CFHTLS using barely resolved galaxies. Figure 1 plots object size measured on the CFHTLS g image (SExtractor’s FLUX_RADIUS) versus magnitude. Astrometric calibrators were selected to have $3.3 < \text{FLUX_RADIUS} < 4.0$ (indicated by the red lines in Figure 1), which avoids stars (the locus of points with $\text{FLUX_RADIUS} \sim 2.7$), but limits the calibrators to barely resolved galaxies, for which accurate centroids can be measured. Calibrators were further required to be clean (based on SExtractor flags) sources with $17.5 < g < 24$. Blended sources were removed by rejecting objects with a neighbour within $2''$. For each CCD, separate affine transformations in right ascension and declination were then fit to the offsets between the CFHTLS and DECam positions. Proper motions were then derived by differencing the CFHTLS and recalibrated DECam positions.

Figure 2 shows the mean and rms differences between the CFHTLS and DECam positions for each CCD before and after the calibrations. Prior to calibrations, the average offsets for each CCD are of order 20 - 150 mas, with RMS of order 50 - 150 mas. After astrometric calibrations, the RMS for each CCD is reduced to ≈ 50 mas.

To estimate proper motion errors as a function of magnitude, we use the RMS of proper motion distributions of barely resolved galaxies at the bright end. We do not use the relatively bright stars for this estimate since the real stellar motions inflate the proper motion RMS. At the faint end, the errors in the centroids of the galaxies inflate the rms, so we use the rms of the proper motion distributions of the stars, which are mostly unaffected by real stellar motions. Proper motion errors are roughly 5 mas yr^{-1} down to $g = 24.5$

¹ <http://www.cfht.hawaii.edu/Science/CFHLS>

² http://ast.noao.edu/sites/default/files/NOAO_DHB_v2.2.pdf

³ <http://www.ipac.caltech.edu/2mass/>

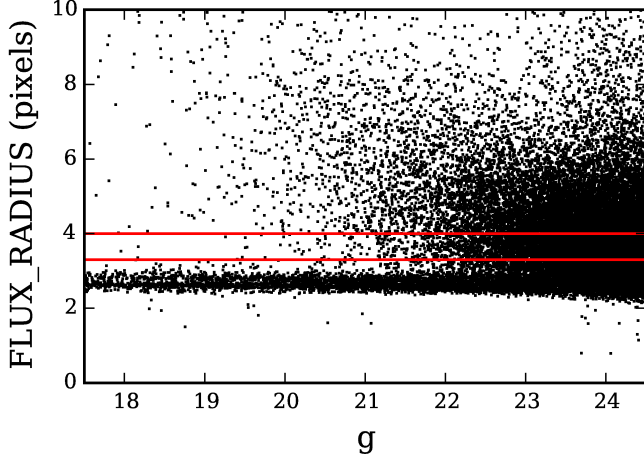


Figure 1. Object size (SExtractor’s FLUX_RADIUS) versus g magnitude, measured on the CFHTLS g image (only 20% of the objects detected have been plotted). The red lines define the band in object size from which astrometric calibrators were selected, corresponding to barely resolved galaxies.

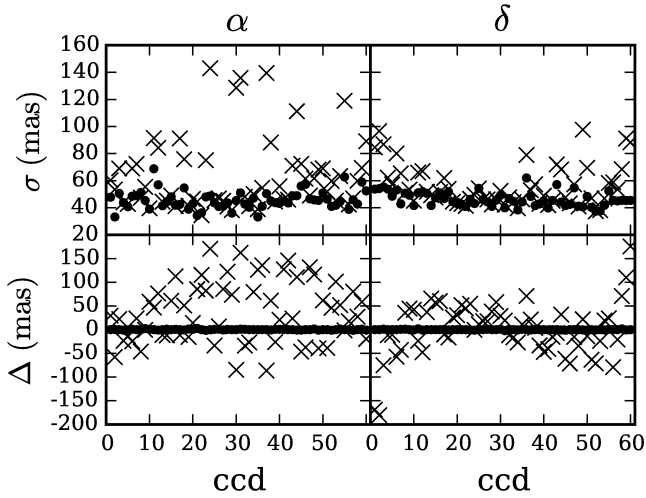


Figure 2. The rms (top panels) and mean (bottom panels) differences between the CFHTLS and DECam positions in right ascension (left panels) and declination (right panels). The crosses are the differences before the recalibration, and the filled circles after the recalibration.

mag. We find $\sigma_\mu = 4.47 \text{ mas yr}^{-1}$ for objects brighter than $g = 21.5 \text{ mag}$, and $\sigma_\mu = 4.69 + 0.183 \times (g - 21.5)^2$ for $g > 21.5 \text{ mag}$. Calibration errors dominate the centroiding errors, even at the faint end.

We compare our proper motion measurements to that of the PPMXL catalog (Roeser, Demleitner & Schilbach 2010). Figure 3 shows this comparison for both before and after the astrometric calibration of our DECam data. The corrected proper motions agree well with the PPMXL values, showing an RMS scatter of 5.3-5.5 mas year^{-1} for stars brighter than $g = 19 \text{ mag}$.

3.2 The Reduced Proper Motion Diagram

Reduced proper motion, defined as $H = m + 5 \log \mu + 5 = M + 5 \log V_{\text{tan}} - 3.379$, can be used as a proxy for absolute magnitude for samples with similar kinematics. It also provides a relatively clean selection of different populations of

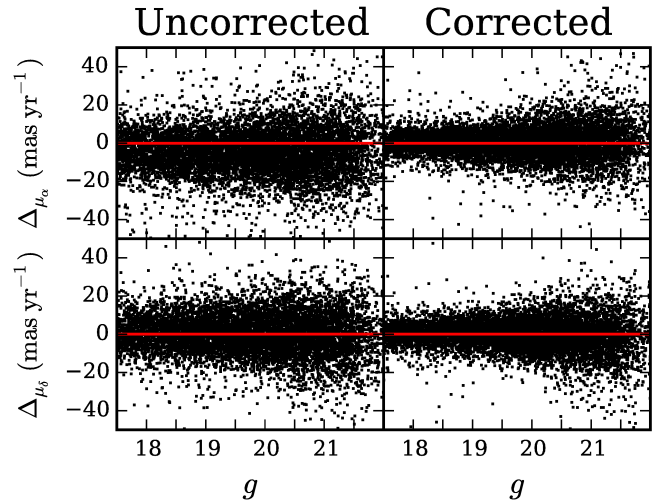


Figure 3. The difference between our proper motions – in both Right Ascension (top) and Declination (bottom) – and the PPMXL catalog. Left panels show the comparison before the astrometric correction, while the right panels show the same comparison after the correction. Our proper motions agree with the PPMXL catalog within 5 mas yr^{-1} for objects brighter than $g = 19 \text{ mag}$.

stars, including white dwarfs and halo subdwarfs (Kilic et al. 2006, 2010).

To generate a clean sample of high proper motion stars, we first apply the cut $2.1 < \text{FLUX_RADIUS} < 3.3$ on the CFHTLS g image, corresponding to the stellar locus in Figure 1. To remove the considerable contamination from galaxies at the faint end, we require a clean, significant proper motion, for which we adopt the following criteria: 1) a one-to-one match between the DECam and CFHT images; 2) a matching distance of less than $4''$, to avoid mismatches; 3) no neighbouring object within $2''$, to avoid blends; 4) ellipticity measured on the DECam image less than 0.2; and 5) a total proper motion of $\mu > 20 \text{ mas yr}^{-1}$, corresponding to roughly a 4σ detection.

Figure 4 shows the reduced proper motion diagram for our first DECam field, along with white dwarf evolutionary tracks for tangential velocities of 20 and 40 km s^{-1} . The red line marks the boundaries for our white dwarf selection region. We visually inspected all objects in this region on both the CFHTLS and DECam images, and classified the likelihood that the proper motion is real. Those objects whose CFHTLS or DECam centroids were clearly wrong (due to such effects as blends with nearby bright stars, false detections due to cosmic rays or diffraction spikes, etc), or whose image profiles are clearly non-stellar, have been rejected and are not plotted. The remaining objects were classified as either “good” or “maybe”. “Good” objects have clean stellar profiles, and their proper motions are likely real. Objects classified as “maybe” are not obviously wrong (e.g., a clear blend with a nearby star), but one or both centroids may be incorrect. Typically one of three concerns was evident on the CFHTLS and/or DECam images: 1) the image profile is slightly asymmetric; 2) there is a nearby neighbor, though not obviously so close as to affect the centroid; or 3) the object is faint enough that it may not be possible to measure an accurate centroid. We suspect that the vast majority of

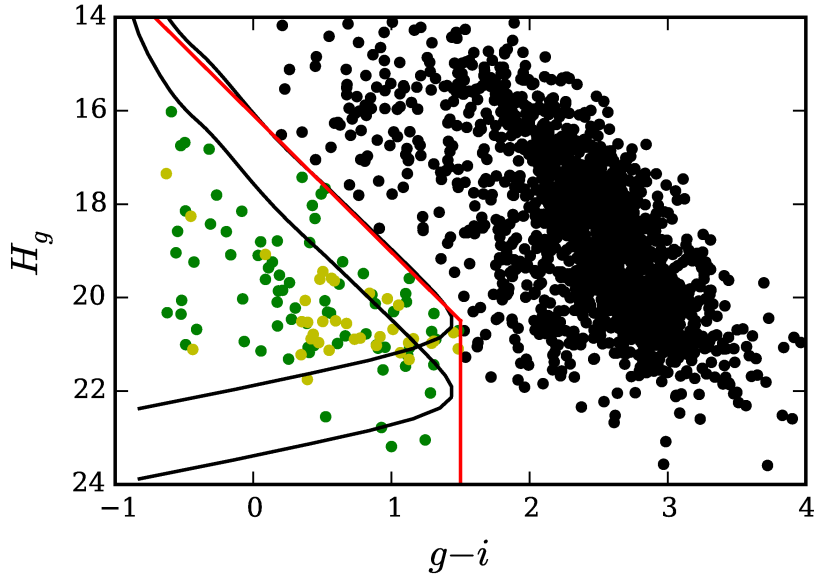


Figure 4. The Reduced Proper Motion diagram for stars in the first DECam field. White dwarf cooling curves for tangential velocities of 20 and 40 km s⁻¹ are shown as solid lines. The red line delineates the area of interest for white dwarfs; we visually inspected each object in this region and classified them as “good” (dark green) and “maybe” (yellow) white dwarf candidates.

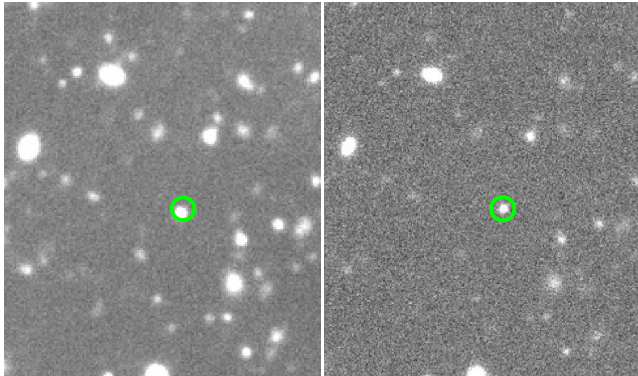


Figure 5. One of the newly identified high proper motion white dwarfs in our program. WD87, J090212.1-051642.7, has $g = 23.7$ mag, and displays a proper motion of 95.3 ± 5.1 mas yr⁻¹. Our stacked DECam image is shown on the left panel, whereas the original CFHTLS image is shown on the right. Green circles mark the position of this object in the CFHTLS data.

the “maybes” have unreliable proper motions, and thus are not white dwarfs (and subsequent analysis in the paper will support this suspicion), however we carry them through the analysis as we also suspect a few may have reliably measured proper motions, and to include them in our photometric analysis in case they show variability or eclipses. We identify 78 good white dwarf candidates and 33 “maybes”.

Figure 5 shows the field around one of the newly identified, good white dwarf candidates in our program, WD87. This figure demonstrates that our stacked DECam image is significantly deeper than the CFHT Legacy Survey data. WD87, J090212.1-051642.7, is relatively faint with $g = 23.7$ mag, but its proper motion is clearly detected between the original CFHT observations and our DECam data from 2014.

3.3 Sample Size

There are 156,325 objects with $g = 17.5 - 24.5$ mag in our field and we classify 59,517 of them as point sources based on their Flux Radius measurements in the 2.1-3.3 pixels range. We lose 14% of the DECam area to trimming, and an additional 9% is lost when performing the 70 pixel cut for the distance of the object from the edge. These cuts are necessary, partly due to the poor quality of the stacked images near the edges and due to the worsening of the astrometric calibration close to the edges. About 7.1% of the remaining stars (hence $\sim 5.5\%$ of the total) in CFHTLS were not detected on the DECam images. Of these, 52% were too close to a large bright object, 40% were blended with a neighbour, and the remaining 8% were affected by image defects. Finally, 4.2% of the remaining stars ($\sim 3\%$ of the original amount) were eliminated due to their nearest neighbour being within $2''$ in either the CFHTLS or the DECam catalog. Therefore the total loss is $\sim 31.5\%$.

The Besançon Galaxy model (Robin et al. 2003) predicts ~ 103 white dwarfs with $g < 24.5$ mag and tangential velocities above 20 km s⁻¹ in our DECam field. Given the 31% loss in our analysis, the expected number of high proper motion white dwarfs is 71. This is similar to the number of white dwarf candidates that we identify based on the reduced proper motion diagram.

Tables 1 and 2 present the coordinates, *ugriz* photometry from the CFHT Legacy Survey, and proper motions for the remaining 78 good white dwarf candidates and 33 MAYBES. The good white dwarf candidates include three objects with $\mu \approx 100$ mas yr⁻¹, WD69, WD73, and WD87, whereas the MAYBES include candidates with total proper motions up to 44 mas yr⁻¹.

Table 2. Astrometry and photometry of the “maybe” white dwarf candidates in the first field.

Target Name	RA (deg)	Dec (deg)	u (mag)	g (mag)	r (mag)	i (mag)	z (mag)	μ_{RA} (mas/year)	μ_{Dec} (mas/year)
WD3	135.942340	-3.675134	23.59±0.04	22.76±0.01	22.26±0.02	22.19±0.03	22.20±0.05	-20.2	-11.6
WD4	136.106871	-3.639555	21.57±0.01	21.57±0.01	21.83±0.01	22.02±0.02	22.38±0.07	7.0	-20.6
WD8	136.300318	-3.798416	24.34±0.13	23.91±0.06	23.26±0.05	23.23±0.10	22.25±0.09	21.2	2.6
WD11	135.132693	-3.937421	23.97±0.08	23.84±0.06	23.46±0.07	23.24±0.06	23.10±0.13	-2.5	-21.3
WD13	135.676317	-3.974249	24.56±0.24	24.30±0.18	22.66±0.06	23.24±0.12	22.28±0.17	5.1	-23.2
WD26	135.258431	-4.386883	24.46±0.18	24.37±0.12	24.27±0.17	23.82±0.12	23.63±0.25	-15.4	-16.4
WD27	135.160187	-4.305303	25.08±0.26	24.18±0.09	24.00±0.12	23.41±0.07	23.21±0.14	18.2	11.9
WD35	135.310004	-4.532012	24.45±0.11	24.41±0.08	24.39±0.18	24.85±0.21	26.20±1.77	7.4	-20.6
WD38	136.217159	-4.511356	23.74±0.12	23.52±0.06	22.99±0.07	23.24±0.15	22.94±0.14	4.5	27.4
WD57	135.082199	-4.867261	24.99±0.19	24.23±0.08	23.33±0.06	22.78±0.05	22.32±0.06	-2.7	-20.0
WD58	135.126308	-4.819013	24.12±0.17	24.36±0.18	19.47±0.00	23.91±0.25	22.98±0.23	30.1	7.6
WD60	135.369363	-4.831089	26.72±0.82	24.32±0.08	23.63±0.08	23.58±0.09	23.49±0.17	-2.6	20.5
WD70	135.772781	-5.053292	24.79±0.11	24.29±0.06	23.53±0.05	23.17±0.05	23.07±0.09	-12.1	-17.9
WD71	135.862551	-4.998320	19.89±0.00	19.87±0.00	20.18±0.00	20.50±0.01	20.72±0.01	-21.4	-22.8
WD72	136.049139	-5.006310	23.51±0.04	22.89±0.02	22.54±0.03	22.41±0.03	22.68±0.08	-20.4	8.2
WD82	136.169766	-5.227046	24.17±0.07	24.08±0.06	23.84±0.08	23.65±0.09	23.69±0.22	-10.6	-19.2
WD85	135.339775	-5.283070	24.41±0.11	24.21±0.07	24.25±0.12	23.79±0.10	23.23±0.14	18.9	-10.5
WD91	135.594910	-4.552363	24.47±0.08	23.27±0.03	22.51±0.02	22.30±0.02	22.23±0.04	-19.6	-10.9
WD92	135.594256	-5.546409	22.51±0.02	22.43±0.01	22.25±0.02	21.92±0.02	21.48±0.03	-18.2	-17.6
WD93	135.587597	-5.445684	24.08±0.10	23.76±0.07	25.67±0.66	23.04±0.07	24.12±0.39	27.1	-0.1
WD99	136.148961	-5.454180	21.13±0.01	20.80±0.00	20.72±0.01	20.71±0.01	20.77±0.02	22.5	-39.2
WD100	136.088231	-5.430176	23.97±0.08	23.14±0.04	22.71±0.05	22.30±0.04	22.52±0.10	-21.9	-5.5
WD101	135.989002	-4.168098	24.01±0.31	22.00±0.03	20.75±0.02	21.01±0.03	20.45±0.03	-13.9	22.7
WD102	135.818565	-4.314596	25.22±0.35	24.11±0.09	23.53±0.09	23.77±0.12	23.92±0.31	21.0	-16.1
WD103	135.086246	-4.525658	24.23±0.10	24.20±0.08	23.96±0.12	23.04±0.05	22.66±0.08	17.6	12.7
WD105	135.863276	-4.860796	23.17±0.03	23.07±0.03	22.83±0.04	22.49±0.03	22.18±0.06	19.0	8.0
WD106	136.108813	-4.887646	23.82±0.06	23.29±0.03	22.90±0.04	22.24±0.03	21.89±0.05	-20.4	11.9
WD107	136.298099	-4.879626	23.30±0.04	23.48±0.04	23.27±0.07	23.10±0.07	23.18±0.18	10.3	-18.0
WD108	136.347112	-4.857691	24.31±0.07	23.90±0.04	23.62±0.06	23.55±0.07	23.58±0.18	-0.5	-21.0
WD109	136.191332	-4.840274	24.23±0.10	24.29±0.10	23.97±0.10	23.37±0.09	23.65±0.26	18.2	-9.2
WD110	136.256013	-5.020012	24.20±0.10	23.71±0.05	22.97±0.05	22.23±0.03	21.76±0.05	-19.8	22.5
WD111	136.212225	-4.929040	23.76±0.06	23.23±0.03	22.81±0.05	22.84±0.05	22.92±0.12	17.2	-23.1
WD112	136.658616	-5.005289	23.41±0.03	22.84±0.02	22.46±0.02	22.33±0.02	22.43±0.06	-33.4	7.9

4 SAMPLE PROPERTIES

4.1 Temperatures and Cooling Ages

Figure 6 displays the $u - g$ versus $g - r$ colour-colour diagram for our white dwarf candidates along with the predicted colours for pure hydrogen atmosphere white dwarfs. The colours for the majority of the good white dwarf candidates are consistent with the models within the errors. On the other hand, a significant fraction of the MAYBEs have redder colours than the models, which could be due to contamination from M dwarf companions or our misidentification of these targets as white dwarfs. Regardless of this issue, our white dwarf candidates show a broad range of colours, indicating a broad range of temperatures, down to the cool white dwarf regime.

We use pure hydrogen and pure helium atmosphere white dwarf models from Bergeron, Wesemael & Beauchamp (1995) and Bergeron et al. (2011) with the improvements discussed in Tremblay & Bergeron (2009) to fit the spectral energy distributions of our targets to constrain their temperatures. Our model grid covers $T_{\text{eff}} = 1500$ to 45,000 K.

Our fitting procedures are described in detail by Gianninas et al. (2015). The only difference here is that due to lack of spectra and parallaxes for our targets, we assume a surface gravity of $\log g = 8.0$. This is acceptable, given that the main peak in the mass distribution of the white dwarfs in the Solar neighbourhood is around $0.6 M_{\odot}$ (Tremblay et al. 2011; Giammichele, Bergeron & Dufour 2012; Limoges, Bergeron & Lépine 2015). Uncertainties

arising from this assumption are further discussed in Section 4.2.

Figure 7 displays representative spectral energy distributions and our pure H and pure He model atmosphere fits to a dozen good white dwarf candidates in our sample. Given the relatively faint magnitudes of our targets, only *ugriz* photometry is available, which limits the choice of composition, especially for cool white dwarfs. Hydrogen-rich white dwarfs below about 5,000 K suffer from collision induced absorption due to molecular hydrogen. Hence, the lack of significant infrared absorption could be a sign of a hydrogen poor atmosphere.

The first two stars in Figure 7, WD32 and WD33, are warmer than about 10,000 K, at which the differences between pure hydrogen and pure helium atmospheres are significant. The spectral energy distributions of these two stars clearly indicate a hydrogen atmosphere white dwarf. On the other hand, the rest of the stars in this figure are cooler than 8,000 K where the differences between the hydrogen and helium atmosphere models in optical photometry is minimal. Without near-infrared photometry, we assume pure hydrogen composition for our targets, unless the spectral energy distribution clearly favors the pure helium atmosphere model. The latter is true for a few of our targets, namely WD68, WD84, WD97, and one of the MAYBEs, WD4.

All but three of the objects in Figure 7 have spectral energy distributions that are well matched by our models. However, the photometry for WD37, WD41, and WD42 is too red to be explained by a single white dwarf. It is possible that these are white dwarf + M dwarf binary systems or they are contaminated by background sources. However,

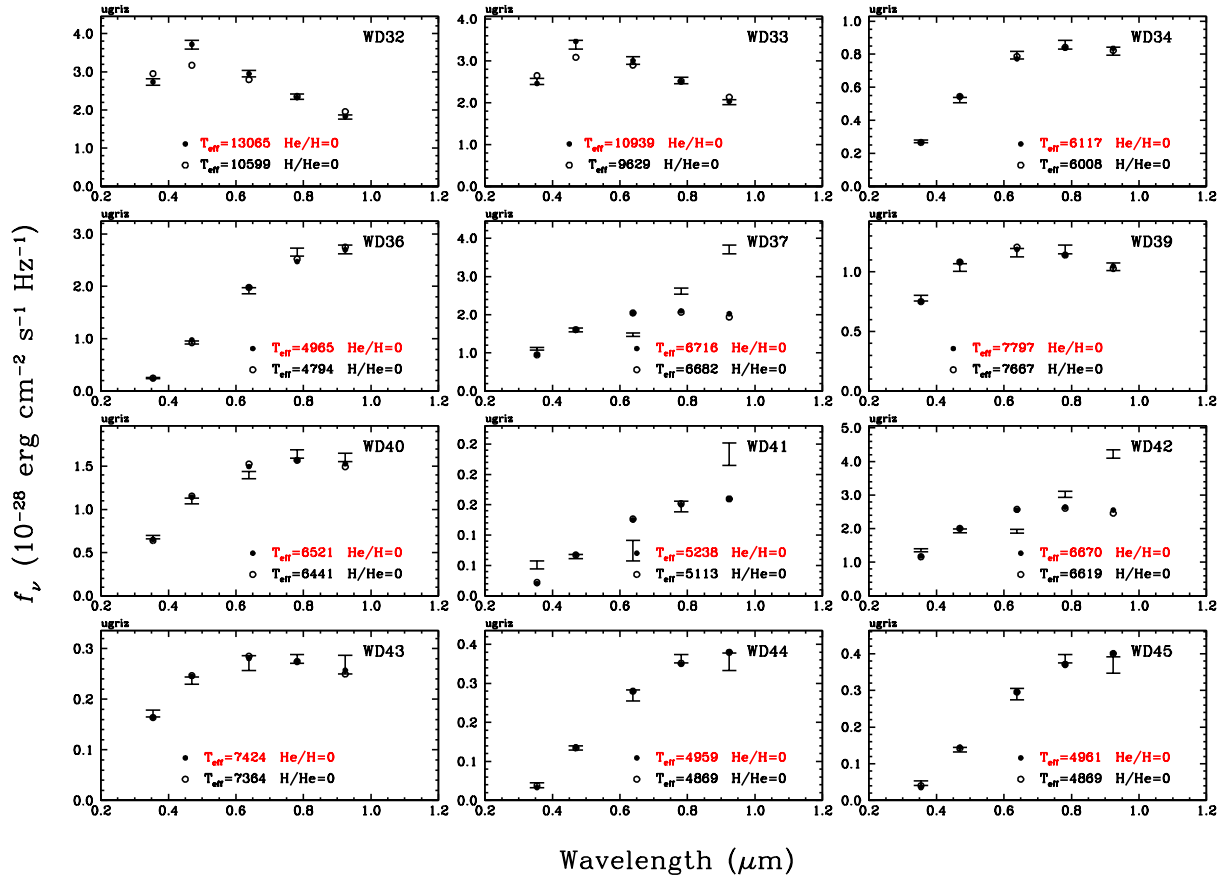


Figure 7. Fits to the observed spectral energy distributions (error bars) of 12 of the good white dwarf candidates with pure hydrogen (filled circles) and pure helium atmosphere models (open circles). The adopted atmospheric parameters are emphasized in red.

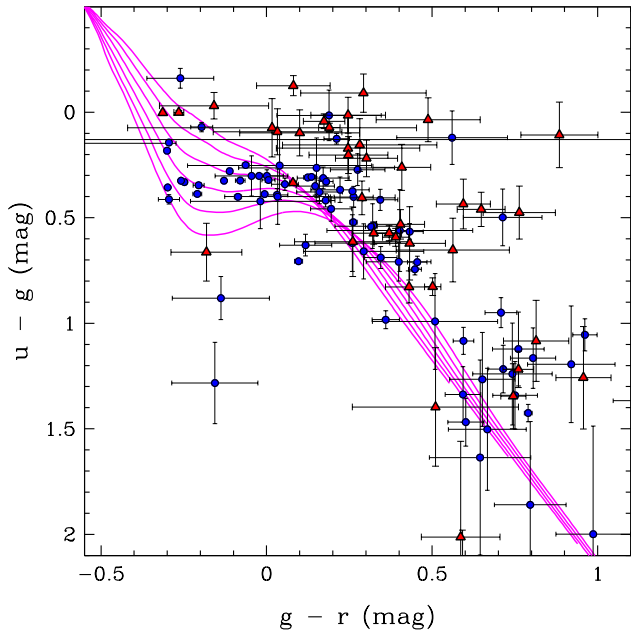


Figure 6. A colour-colour diagram for our proper motion selected sample of white dwarfs. The colours for “good” (blue circles) and “maybe” (red triangles) white dwarf candidates along with the predicted colours for pure hydrogen atmospheres with $\log g = 7.0$ to 9.5 and T_{eff} from 120,000 to 1500 K are also shown.

all three of these targets look like point sources, and we detect $>20 \text{ mas yr}^{-1}$ proper motions. In addition, one of these sources, WD42, is a variable object with pulsation periods of 11-13 min, which demonstrate that it is a pulsating ZZ Ceti white dwarf (see Section 5.2) likely in a white dwarf + M dwarf system (Pyrzas et al. 2015). Thus, we favour the stellar binary explanation for these sources.

Tables 3 and 4 include temperature, distance, age, and tangential velocity estimates for our white dwarf candidates. Our sample includes white dwarfs with $T_{\text{eff}} = 22,150 \text{ K}$ down to 4250 K, which correspond to cooling ages of up to 8.4 Gyr for $\log g = 8$ white dwarfs. The estimated distances range from 147 pc to 4.9 kpc.

4.2 Kinematic Properties: Halo versus Disk

Figure 8 presents tangential velocities and cooling ages for our high proper motion white dwarf candidates. There are two candidates, WD87 and WD35 (which is classified as a MAYBE), with tangential velocities larger than the escape speed from the Galaxy.

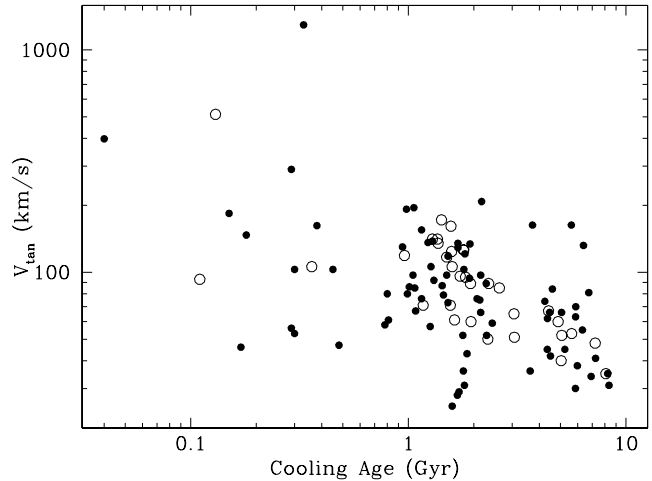
Both velocities and cooling ages strongly depend on the choice of mass, or surface gravity for our targets. The white dwarf mass distribution peaks at about $0.6 M_{\odot}$ and there is another peak at lower masses ($0.4 M_{\odot}$) and a tail toward higher masses (Tremblay et al. 2013). Hence, our choice of $\log g = 8$ is appropriate for most targets, and for studying

Table 3. Physical parameters of the good white dwarf candidates in the first field. Here and in Table 4 we assume a surface gravity of $\log g = 8$.

Target Name	T_{eff} (K)	Distance (pc)	Age (Gyr)	V_{tan} (km s^{-1})
WD1	5960±220	853	2.28	89
WD2	16200±800	1776	0.15	184
WD5	15600±620	297	0.17	46
WD6	11140±430	641	0.45	103
WD7	4290±150	322	8.24	35
WD9	8260±300	758	0.99	80
WD10	6510±260	803	1.82	121
WD12	13040±660	842	0.30	103
WD14	7790±670	1368	1.15	155
WD15	6100±370	1005	2.15	97
WD16	4250±190	326	8.36	31
WD17	5390±80	342	3.63	36
WD18	5230±100	411	4.50	42
WD19	5020±230	597	5.61	163
WD20	13190±620	508	0.29	56
WD21	11970±680	1195	0.38	162
WD22	8920±310	531	0.81	61
WD23	7000±550	1231	1.52	118
WD24	6710±160	696	1.69	135
WD25	22150±2030	3715	0.04	398
WD28	7140±160	534	1.45	79
WD29	5090±90	365	5.24	45
WD30	4600±110	352	7.25	41
WD31	7980±240	664	1.08	67
WD32	13070±640	502	0.30	53
WD33	10940±410	432	0.48	47
WD34	6120±70	357	2.13	75
WD36	4970±50	147	5.86	30
WD37	6720±130	256	1.68	28
WD39	7800±210	423	1.15	76
WD40	6520±100	285	1.81	31
WD41	5240±200	658	4.46	66
WD42	6670±120	226	1.71	29
WD43	7430±230	807	1.31	92
WD44	4960±120	391	5.88	70
WD45	4960±120	381	5.87	63
WD46	8000±220	434	1.07	85
WD47	7510±310	959	1.27	106
WD48	5950±60	334	2.29	52
WD49	5260±70	302	4.35	45
WD50	7000±220	766	1.52	73
WD51	6540±380	1055	1.80	103
WD52	8070±260	759	1.05	97
WD53	7160±260	844	1.43	87
WD54	5830±140	564	2.43	59
WD55	4940±90	357	5.98	38
WD56	5130±200	619	5.06	66
WD59	6380±90	285	1.91	94
WD61	4700±80	268	6.92	34
WD62	6870±120	205	1.59	25
WD63	7470±690	1450	1.29	138
WD64	6710±180	721	1.69	129
WD65	5260±210	602	4.36	62
WD66	6070±170	710	2.17	208
WD67	7600±350	954	1.23	136
WD68	9390±240	388	0.78	58
WD69	13170±630	601	0.29	290
WD73	15370±620	261	0.18	147
WD74	5280±190	626	4.24	74
WD75	6100±100	550	2.15	66
WD76	6190±90	514	2.07	76
WD77	8050±1000	1692	1.06	195
WD78	6550±100	318	1.79	36
WD79	6570±120	511	1.78	52
WD80	6380±330	1049	1.92	134
WD81	4850±220	543	6.38	132
WD83	7030±260	893	1.50	97
WD84	9270±230	474	0.80	80
WD86	5380±260	741	3.72	163
WD87	12500±2940	2855	0.33	1295
WD88	4750±190	494	6.75	81
WD89	4860±200	521	6.31	55
WD90	7530±190	471	1.26	57
WD94	6460±90	360	1.86	43
WD95	5220±90	389	4.59	84
WD96	8430±270	586	0.94	130
WD97	8510±210	525	1.01	86
WD98	8280±1360	1764	0.98	192

Table 4. Physical parameters of the “maybe” white dwarf candidates in the first field.

Target Name	T_{eff} (K)	Distance (pc)	Age (Gyr)	V_{tan} (km s^{-1})
WD3	5930±80	448	2.32	50
WD4	12570±520	1019	0.36	106
WD8	5540±200	637	3.06	65
WD11	6650±280	940	1.73	96
WD13	5720±270	748	2.62	85
WD26	6560±460	1176	1.79	126
WD27	5910±260	857	2.34	89
WD35	17120±3870	4923	0.13	513
WD38	6540±340	958	1.80	126
WD57	4340±160	362	8.09	35
WD58	7180±510	1167	1.42	172
WD60	5250±220	685	4.41	67
WD70	7320±550	1193	1.36	141
WD71	5160±170	578	4.88	60
WD72	17620±750	627	0.11	93
WD82	6360±100	543	1.93	89
WD85	7460±580	1347	1.29	141
WD91	6890±470	1204	1.58	124
WD92	5130±80	375	5.04	40
WD93	6810±140	509	1.63	61
WD99	7300±440	1048	1.37	135
WD100	7750±200	330	1.17	71
WD101	5120±100	408	5.07	52
WD102	6910±520	1283	1.57	161
WD103	5010±180	516	5.63	53
WD105	6930±170	725	1.56	71
WD106	5530±90	457	3.07	51
WD107	8370±600	1211	0.96	119
WD108	6870±340	1056	1.59	106
WD109	7040±540	1202	1.50	117
WD110	6350±110	577	1.94	60
WD111	4610±110	333	7.22	48
WD112	6490±190	696	1.83	95

**Figure 8.** Tangential velocity versus age for the good (filled) and probable (open circles) white dwarf candidates in the first field. Both V_{tan} and the cooling age strongly depend on the mass of the white dwarf, which is assumed to be $M \approx 0.6M_{\odot}$ (i.e., $\log g = 8$) in this analysis.

the ensemble properties, but the cooling ages and especially tangential velocities may be skewed toward higher values if the surface gravity is significantly different. For example, at $T_{\text{eff}} = 12,000\text{K}$, increasing the assumed surface gravity by 1 dex lowers the distance estimate and thus the tangential velocity by a factor of two. Hence, WD87 and WD35 are likely more massive than the canonical $0.6 M_{\odot}$, as it is highly un-

likely to find two such objects in our relatively small sample of white dwarfs.

Figure 8 surprisingly shows a trend in which younger objects tend to have higher tangential velocities. This is highly unexpected, as halo objects (therefore older and cooler white dwarfs) should have larger tangential velocities. Particularly, WD25 has a tangential velocity of 400 km s^{-1} , and a cooling age of only 40 million years. It is possible that WD25 could be a newly born halo white dwarf with $M \approx 0.53 M_{\odot}$ (Bergeron, Leggett & Ruiz 2001). However, this would be a rare occurrence, since most of the halo population is old. The Besançon Galaxy model (Robin et al. 2003) predicts 0-1 halo white dwarfs in our field down to $g = 24.5$ mag. Some of the fastest moving objects could in fact still belong to the Galactic disc, but have a $\log g > 8.0$.

Given the significant errors on the estimated distances, the tangential velocity distribution is predicted to range between 19 and 110 km s^{-1} for the thin disk and between 53 and 133 km s^{-1} for the thick disk populations. Moreover, the thick disk white dwarfs are predicted to be outnumbered by the thin disk sample by a factor of 15. The majority of the objects in our sample have tangential velocities $< 200 \text{ km s}^{-1}$, thus are consistent with Galactic disk membership.

5 THE LIGHT CURVES

5.1 Building the Light Curves

In order to generate lightcurves for all of the white dwarf targets, we used the IRAF *phot* package to perform aperture photometry on all of the images collected with DECam. Since we are interested in identifying variable objects, only relative photometry is needed for our program, and we do not perform absolute photometric calibration of our DECam observations.

To account for short-term changes in the atmosphere (such as cloud coverage or haze), as well as the change in airmass, we use six bright, unsaturated, non-variable stars in each CCD as reference stars. Given the large field of view of DECam, the image quality differs for different CCDs. Hence, the selection of reference stars and our calibration procedures are done separately for each CCD. After shifting the six reference stars to the same magnitude scale, we use a sigma-clipping algorithm to reject bad points that are affected by cosmic rays or CCD defects, and we take their weighted mean to create a reference light curve for each CCD. To calibrate the relative photometry for our white dwarf targets, we subtract the appropriate calibration light curve, given the CCD that includes each target. Note that this process was run separately for each night, and for each CCD that contained one or more targets.

The reference stars chosen to calibrate the light curves are typically redder than our white dwarf targets. Hence, airmass related effects are still present in the light curves of many of our targets and they lead to significant peaks especially at 4 cycles per day in the Fourier Transforms. We fitted third degree polynomials to the target light curves to remove this effect.

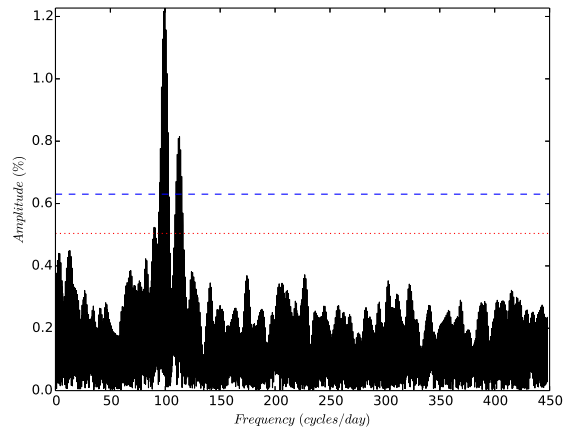


Figure 10. Fourier transform of the WD42 light curve. The red dotted line and the blue dashed line show the $4 \langle A \rangle$ and $5 \langle A \rangle$ detection limits, respectively. There are two significant peaks, indicating pulsation frequencies of 99.6 and $112.9 \text{ cycles day}^{-1}$.

5.2 A New Variable System

We use the Period04⁴ package to calculate Discrete Fourier Transforms for each of our white dwarf targets. We compare the amplitudes of the observed peaks with the median amplitude ($\langle A \rangle$) in the Fourier Transform, and only consider the peaks above $5 \langle A \rangle$ as significant. Some of our targets still show significant peaks at 4, 6, 8, or 12 cycles per day due to our observing window. However, there is only one target that is clearly variable.

Figure 9 shows the 8-night-long light curve of WD42. Sinusoidal variations in each night are clearly visible in this light curve. Figure 10 shows the Fourier Transform of this light curve. There are two significant peaks at 99.5889 ± 0.0069 and 112.9466 ± 1.8662 cycles per day with amplitudes of $1.22 \pm 0.12\%$ and $0.79 \pm 0.25\%$, respectively. The observed range of periods, 765-868 s, are consistent with the pulsation periods seen in ZZ Ceti white dwarfs (e.g., Mukadam et al. 2004).

ZZ Ceti white dwarfs are found in a narrow instability strip around $T_{\text{eff}} \approx 12,000 \text{ K}$ (Gianninas, Bergeron & Ruiz 2011). However, our model fits to the spectral energy distribution of WD42 (see Fig. 7) indicate an effective temperature of 6670 K for a single white dwarf. These models clearly fail to reproduce the spectral energy distribution of WD42. A likely explanation for the observed colours of WD42 is that it is a pulsating white dwarf + M dwarf system in which the white dwarf dominates the photometry in the blue (ug bands) and the M dwarf dominates in the red. With an apparent magnitude of $g = 20.64$, WD42 becomes the second faintest pulsating white dwarf known after the white dwarf companion of PSR J1738+0333 (Kilic et al. 2015).

5.3 No Transits

Solid body transits around white dwarfs last 1-2 min (e.g. Brown et al. 2011). Hence, such events would affect only

⁴ <https://www.univie.ac.at/tops/Period04/>

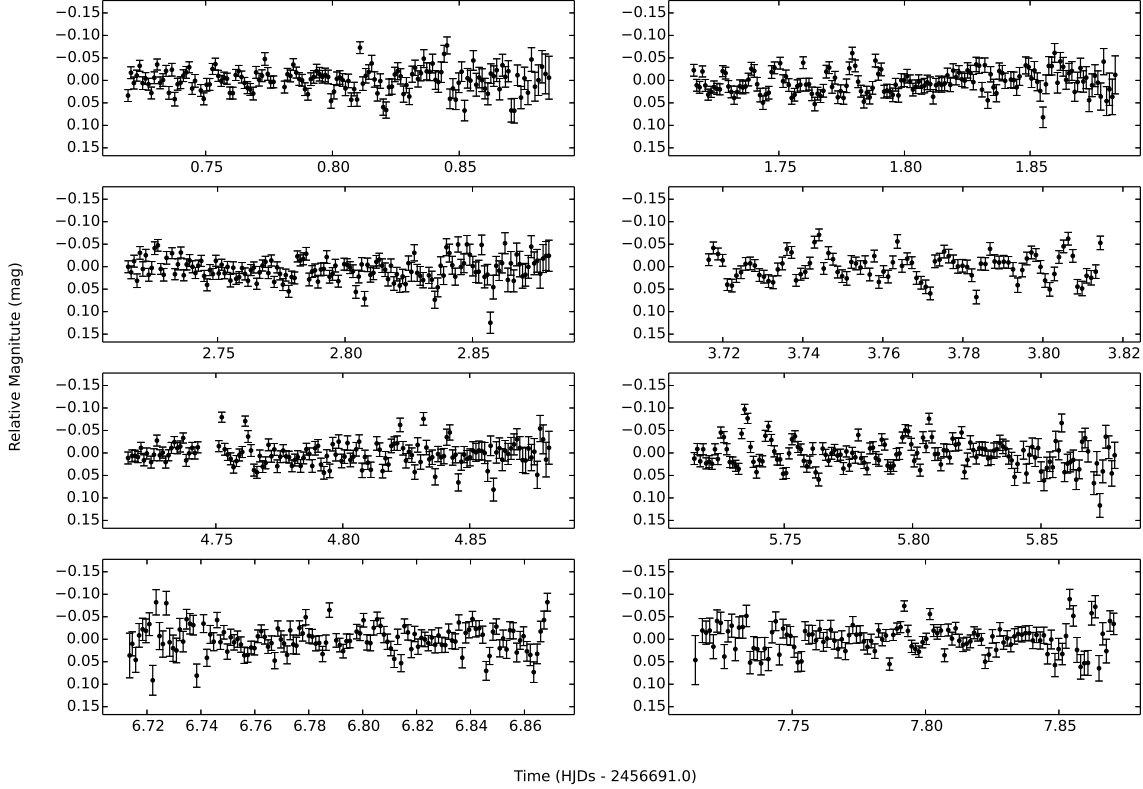


Figure 9. DECcam time-series photometry of WD42 over 8 half-nights. The lightcurve shows significant sinusoidal variations, especially visible in nights two and four, making this one of the faintest ZZ Ceti white dwarfs currently known.

one or two photometric points for each orbital period. After constructing 8-night-long lightcurves for all of the white dwarf candidates and MAYBEs, we checked all of them for the presence of significant ($\geq 4\sigma$) dips, and we visually inspected the images with potential transits. One of our targets, WD46, showed significant photometric dips at the end of the night, for several nights. A careful inspection of the images with the dips show that WD46 is close to the edge of the chip and the point spread function is rather elliptical at its location in these images. Hence, the observed photometric dips are not real. None of the remaining targets show any significant dips that could be attributed to an eclipsing planet orbiting around its host star.

Given our 4 h long observing window each night, we are sensitive to 100% of transiting objects with orbital periods of 4 h or less, assuming they cause significant eclipses. However, we expect the detection rate to fall significantly at longer orbital periods, and especially at 6, 8, 12, 16, 24 and 28 h, which are discrete frequencies of our observing window of 4 h per night.

To estimate our transit detection efficiency, we simulate an 8-day-long set of lightcurves, each with cadences of 90 seconds, presenting eclipses the length of one data point at periods ranging from 2 to 30 hours, with increments of 30 minutes. We then filter the light curves through our observing window and shift the times of eclipses to probe all pos-

sible configurations. We require at least two eclipse events to call it a detection.

Figure 11 presents the transit detection probability for a flat distribution of periods. We see an overall trend of decreasing probability as the orbital period increases. The total shaded area in the graph represents the cumulative probability of detecting a transiting object in the sample, which corresponds to 68.5%. In other words, our DECcam observations are capable of detecting 68.5% of the significant transits with periods less than 30 h. The detectability of a given planet depends on the magnitude of its host star. Dimmer stars show higher scatter in their light curves, and this limits the detection of asteroids and moons around the fainter targets. Table 5 shows the minimum depth (in percentage) required for eclipses to be detected at the 4σ level when probing stars of different magnitudes. Assuming that the majority of our targets are average mass white dwarfs with a radius comparable to Earth, our observations are sensitive to transits by moon-sized objects for targets brighter than $g = 20$ mag, and by Earth-sized objects for all targets.

The probability of an eclipse is 1% for an Earth-like planet orbiting in the habitable zone of a white dwarf, which typically extends between 0.005 and 0.02 AU for a $0.6 M_{\odot}$ white dwarf (Agol 2011). Therefore, our cumulative detection rate corresponds to an expected detection rate of 0.7% due to our observing window from the ground. Hence, we would expect to find 0.8 planets in a sample of 111 stars, if

Table 5. Minimum detectable transit depth for a variety of magnitudes present in our sample

Target Name	Magnitude (mag)	Minimum Transit Depth (%)
WD73	18.22	2.7
WD33	20.04	7.5
WD12	21.09	11.1
WD34	22.10	36.7
WD79	22.58	51.0
WD50	23.01	63.2
WD23	24.03	86.4
WD81	24.50	92.6

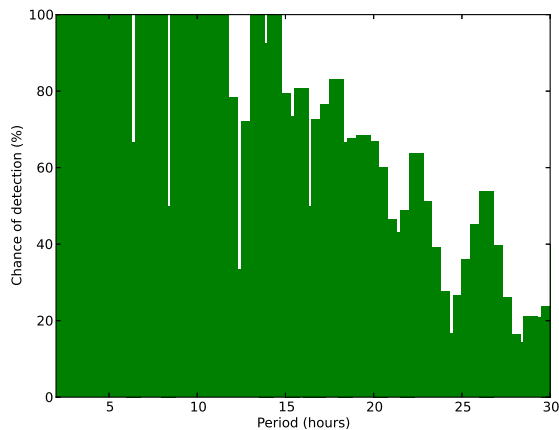


Figure 11. The probability of transit detection (green area) as a function of the orbital period based on our cadence and observing window of 8 half-nights. The range of periods covers the extent of the Habitable Zone of a $0.6 M_{\odot}$ white dwarf. The cumulative detection rate for $P \leq 30$ h is 68.5%.

each white dwarf had an earth-mass planetary companion within its habitable zone. Therefore, the lack of detection of eclipses in our sample of 111 white dwarf candidates is not surprising.

6 CONCLUSIONS

We present the results from the first minute-cadence survey of a large number of white dwarf candidates observed with DECam. We identify 111 high proper motion white dwarf candidates brighter than $g = 24.5$ mag in a single DECam pointing. We estimate temperatures, cooling ages, and tangential velocities for each object and demonstrate that our targets are consistent with thin and thick disk white dwarfs.

We create light curves for each white dwarf, spanning 8 half-nights. We identify a $g = 20.64$ mag pulsating ZZ Ceti white dwarf, most likely in a binary system with an M dwarf companion. We do not find any eclipsing systems in this first field, but given the probability of eclipses of 1% and our observing window from the ground, this is not surprising. However, this work demonstrates the feasibility of using DECam to search for minute-cadence transits around white dwarfs. In addition to the high proper motion white dwarfs, the Besançon Galaxy model predicts 400 other white dwarfs with $\mu < 20$ mas yr⁻¹ in one of our DECam fields.

Image subtraction routines can be used to search for variability for all of the sources in our DECam field, including the non-moving white dwarfs. Such a study with High Order Transform of PSF and Template Subtraction (HOTPANTS, Becker 2015) is currently underway and it will be presented in a future publication. Given the probability of 0.7% of finding a transit around a white dwarf, increasing the size of the white dwarf sample to several hundreds would enable us to find the first solid-body planetary companion, if such systems exist.

ACKNOWLEDGEMENTS

We gratefully acknowledge the support of the NSF and NASA under grants AST-1312678 and NNX14AF65G, respectively. Based on observations at Cerro Tololo Inter-American Observatory, National Optical Astronomy Observatory (NOAO Prop. ID: 2014A-0073; PI: M. Kilic), which is operated by the Association of Universities for Research in Astronomy (AURA) under a cooperative agreement with the National Science Foundation. This project used data obtained with the Dark Energy Camera (DECam), which was constructed by the Dark Energy Survey (DES) collaboration. Funding for the DES Projects has been provided by the U.S. Department of Energy, the U.S. National Science Foundation, the Ministry of Science and Education of Spain, the Science and Technology Facilities Council of the United Kingdom, the Higher Education Funding Council for England, the National Center for Supercomputing Applications at the University of Illinois at Urbana-Champaign, the Kavli Institute of Cosmological Physics at the University of Chicago, the Center for Cosmology and Astro-Particle Physics at the Ohio State University, the Mitchell Institute for Fundamental Physics and Astronomy at Texas A&M University, Financiadora de Estudos e Projetos, Fundação Carlos Chagas Filho de Amparo à Pesquisa do Estado do Rio de Janeiro, Conselho Nacional de Desenvolvimento Científico e Tecnológico and the Ministério da Ciência, Tecnologia e Inovação, the Deutsche Forschungsgemeinschaft, and the Collaborating Institutions in the Dark Energy Survey. The Collaborating Institutions are Argonne National Laboratory, the University of California at Santa Cruz, the University of Cambridge, Centro de Investigaciones Energéticas, Medioambientales y Tecnológicas-Madrid, the University of Chicago, University College London, the DES-Brazil Consortium, the University of Edinburgh, the Eidgenössische Technische Hochschule (ETH) Zürich, Fermi National Accelerator Laboratory, the University of Illinois at Urbana-Champaign, the Institut de Ciències de l'Espai (IEEC/CSIC), the Institut de Física d'Altes Energies, Lawrence Berkeley National Laboratory, the Ludwig-Maximilians Universität München and the associated Excellence Cluster Universe, the University of Michigan, the National Optical Astronomy Observatory, the University of Nottingham, the Ohio State University, the University of Pennsylvania, the University of Portsmouth, SLAC National Accelerator Laboratory, Stanford University, the University of Sussex, and Texas A&M University.

REFERENCES

- Agol E., 2011, *ApJ*, 731, L31
- Alcock C. et al., 2000, *ApJ*, 542, 281
- Becker A., 2015, HOTPANTS: High Order Transform of PSF ANd Template Subtraction. Astrophysics Source Code Library
- Bergeron P., Leggett S. K., Ruiz M. T., 2001, *ApJS*, 133, 413
- Bergeron P., Wesemael F., Beauchamp A., 1995, *PASP*, 107, 1047
- Bergeron P. et al., 2011, *ApJ*, 737, 28
- Bernstein J. P. et al., 2012, *ApJ*, 753, 152
- Bertin E., Arnouts S., 1996, *AAp&S*, 117, 393
- Brown W. R., Kilic M., Hermes J. J., Allende Prieto C., Kenyon S. J., Winget D. E., 2011, *ApJ*, 737, L23
- Debes J. H., Walsh K. J., Stark C., 2012, *ApJ*, 747, 148
- Drake A. J. et al., 2009, *ApJ*, 696, 870
- Flaugher B., 2005, *International Journal of Modern Physics A*, 20, 3121
- Gänsicke B. T. et al., 2016, *ApJ*, 818, L7
- Giammichele N., Bergeron P., Dufour P., 2012, *ApJS*, 199, 29
- Gianninas A., Bergeron P., Ruiz M. T., 2011, *ApJ*, 743, 138
- Gianninas A., Curd B., Thorstensen J. R., Kilic M., Bergeron P., Andrews J. J., Canton P., Agüeros M. A., 2015, *MNRAS*, 449, 3966
- Ivezić Ž. et al., 2007, *AJ*, 134, 973
- Jura M., 2003, *ApJ*, 584, L91
- Kaiser N. et al., 2010, in *Society of Photo-Optical Instrumentation Engineers (SPIE) Conference Series*, Vol. 7733, *Society of Photo-Optical Instrumentation Engineers (SPIE) Conference Series*, p. 0
- Kilic M., Hermes J. J., Gianninas A., Brown W. R., 2015, *MNRAS*, 446, L26
- Kilic M. et al., 2010, *ApJS*, 190, 77
- Kilic M. et al., 2006, *AJ*, 131, 582
- Limoges M.-M., Bergeron P., Lépine S., 2015, *ApJS*, 219, 19
- Monet D. G. et al., 2003, *AJ*, 125, 984
- Mukadam A. S., Winget D. E., von Hippel T., Montgomery M. H., Kepler S. O., Costa A. F. M., 2004, *ApJ*, 612, 1052
- Pyrzas S. et al., 2015, *MNRAS*, 447, 691
- Rappaport S., Gary B. L., Kaye T., Vanderburg A., Croll B., Benni P., Foote J., 2016, *MNRAS*, 458, 3904
- Rau A. et al., 2009, *PASP*, 121, 1334
- Robin A. C., Reylé C., Derrière S., Picaud S., 2003, *A&A*, 409, 523
- Roeser S., Demleitner M., Schilbach E., 2010, *AJ*, 139, 2440
- Tonry J. L. et al., 2012, *ApJ*, 745, 42
- Tremblay P.-E., Bergeron P., 2009, *ApJ*, 696, 1755
- Tremblay P.-E., Ludwig H.-G., Steffen M., Bergeron P., Freytag B., 2011, *A&A*, 531, L19
- Tremblay P.-E., Ludwig H.-G., Steffen M., Freytag B., 2013, *A&A*, 559, A104
- Udalski A., 2003, *ACA*, 53, 291
- Vanderburg A. et al., 2015, *Nature*, 526, 546
- Veras D., Mustill A. J., Bonsor A., Wyatt M. C., 2013, *MNRAS*, 431, 1686

This paper has been typeset from a \TeX / \LaTeX file prepared by the author.